

BER Analysis and Optimization for Continuous RIS-Enabled NOMA

Mahmoud AlaaEldin, *Member, IEEE*, Amy S. Inwood, *Member, IEEE*,
Peter J. Smith, *Fellow, IEEE*, and Michail Matthaiou, *Fellow, IEEE*

Abstract—This letter investigates a novel uplink (UL) system that integrates power-domain non-orthogonal multiple access (PD-NOMA) with a continuous reconfigurable intelligent surface (CRIS). We analyze the effective CRIS-assisted channels under spatially correlated fading to accurately approximate the characteristic function of the cascaded channel. This allows the derivation of an expression for the bit error rate (BER), a key performance metric for UL PD-NOMA. We further utilize the derived BER expressions to introduce a joint optimization framework that minimizes the average BER via UL power allocation and dynamic RIS partitioning among the users. The analytical results are validated by simulations, and show that the proposed optimization scheme eliminates the BER floors that are associated with UL NOMA. The results also confirm the superiority of the optimized CRIS-NOMA scheme over conventional orthogonal multiple access (OMA) and non-optimized UL NOMA schemes.

Index Terms—Continuous RIS, joint power and RIS area optimization, statistical analysis, uplink NOMA.

I. INTRODUCTION

The demand for mobile connectivity continues to grow rapidly, driven by increasingly data-intensive applications, such as high-definition video streaming, augmented reality, and artificial intelligence. However, mobile network resources, such as spectrum and power, are fundamentally limited. To meet this growing demand, it is essential to improve the efficiency with which existing resources are utilized.

One promising technology proposed to address this challenge is non-orthogonal multiple access (NOMA) [1], which allows multiple user equipment (UEs) to simultaneously share the same resource block. In contrast, traditional orthogonal multiple access (OMA) schemes divide the available resources among UEs, thereby reducing the portion each UE can access.

Continuous aperture surfaces, such as holographic reconfigurable intelligent surfaces (HRISs) [2]–[4] and continuous aperture arrays (CAPAs) [5], [6], have significant potential to enhance the performance of NOMA systems with minimal power consumption. By manipulating the propagation environment, these surfaces can be employed to strengthen the power-domain (PD) separation between UEs, improving the overall efficiency of PD-NOMA. Continuous aperture surfaces have demonstrated superior performance compared to discrete counterparts [7], offering enhanced beam steering precision

This work was supported by the U.K. Engineering and Physical Sciences Research Council (EPSRC) grant (EP/X04047X/2) for TITAN Telecoms Hub. The work of P. J. Smith was supported by the Marsden Fund Council from New Zealand Government funding, managed by Royal Society Te Apārangi. The work of M. Matthaiou was supported by the European Research Council (ERC) under the European Union’s Horizon 2020 research and innovation programme (grant agreement No. 101001331).

M. AlaaEldin, A. S. Inwood, and M. Matthaiou are with the Centre for Wireless Innovation (CWI), Queen’s University Belfast, Belfast BT3 9DT, U.K. (e-mail: {m.alaeldin, a.inwood, m.matthaiou}@qub.ac.uk).

P. J. Smith is with the School of Mathematics and Statistics, Victoria University of Wellington, Wellington, New Zealand (e-mail: peter.smith@vuw.ac.nz).

and improved utilization of the full physical aperture for energy capture. Existing work on the symbiosis of continuous aperture surfaces and NOMA focuses mainly on downlink (DL) HRIS-enabled NOMA systems. For this scenario, [2] and [3] derived the outage probability for perfect and imperfect successive interference cancellation (SIC), respectively, while [4] explored the block error rate.

To date, there have been no studies on the uplink (UL) or symbol-level performance of continuous aperture surface-aided NOMA systems. Therefore, this letter presents the first results on both topics. We build upon the foundational work in [8], which studied the bit error rate (BER) of an UL NOMA system with a discrete RIS (DRIS) under uncorrelated channel conditions. Here, we significantly extend this work to a NOMA scenario involving a continuous RIS (CRIS) [9] and the more realistic case of spatially correlated channels. CRISs differ slightly from HRISs and DRISs: a DRIS consists of individually controllable spatially separated elements that form a finite physical aperture, an HRIS consists of densely packed, electromagnetically coupled elements that form a spatially continuous aperture [3], whereas a CRIS assumes a truly continuous distribution across the aperture [9]. The benefits of studying CRISs are twofold: the derived results serve both as a model for truly continuous surfaces and as an upper bound on the performance of discrete RISs when the element density increases. Considering spatially correlated channels is particularly important for CRIS systems, as the infinite element density of a CRIS implies that many pairs of points lie within the channel’s decorrelation distance.

The main contributions of this work are as follows:

- The received signal of the partitioned CRIS NOMA system is expressed in terms of effective channel components, for which we derive the first and second moments.
- Using these results, we derive the cascaded channel characteristic function (CF) required to compute the BER, a critical metric for UL PD-NOMA due to the error floor.
- We propose a joint optimization method for UL power allocation (PA) and CRIS partitioning to minimize BER.

Notation: The statistical expectation is denoted $\mathbb{E}[\cdot]$; $\text{Var}[\cdot]$ is the variance; $\mathcal{CN}(\mu, \sigma^2)$ denotes a complex Gaussian distribution with mean μ and variance σ^2 ; $\Re z$ and $\Im z$ are the real and imaginary components of a complex number z , respectively; $(\cdot)^*$ represents the complex conjugate operator; $\angle z$ is the angle of a complex number z ; ${}_2F_1(\cdot)$ is the Gaussian hypergeometric function.

II. SYSTEM MODEL

We consider the UL system in Fig. 1, where K single-antenna UEs, U_1 to U_K , communicate with a single-antenna base station (BS) via a passive, rectangular CRIS of width W and height H , upon which every point can effect the desired

phase shift.¹ We assume that the direct path between the UEs and BS is fully obstructed, as commonly assumed in the RIS literature [2]–[4], [8]. The CRIS is partitioned into K vertical sections, \mathcal{P}_1 through \mathcal{P}_K . Each partition \mathcal{P}_k spans the full height H and has width W_k . The phase shifts of all points $(x_k, y_k) \in \mathcal{P}_k$ are designed to enhance the channel of U_k .

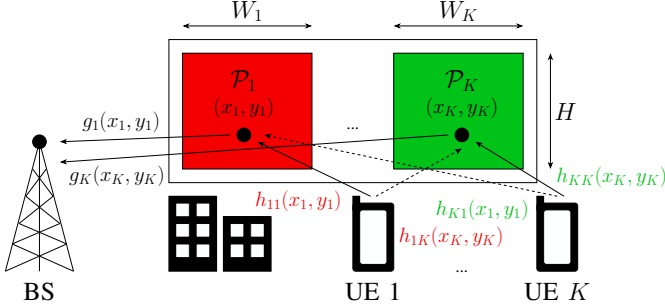


Fig. 1. A CRIS-enabled UL NOMA system.

Let $h_{ki}(x_i, y_i) \in \mathbb{C}$ be the normalized channel from U_k to position $(x_i, y_i) \in \mathcal{P}_i$ on the CRIS, and $g_i(x_i, y_i) \in \mathbb{C}$ be the normalized channel from $(x_i, y_i) \in \mathcal{P}_i$ to the BS. We assume spatially correlated Rayleigh fading so that channels corresponding to any two points (x_i, y_i) and (x_k, y_k) on the CRIS are both $\mathcal{CN}(0, 1)$ with correlation $\rho(x_i, y_i, x_k, y_k)$. We naturally assume that all UE-CRIS channels are statistically independent of all CRIS-BS channels. Let $\Phi_k(x_k, y_k)$ be the CRIS reflection coefficient at $(x_k, y_k) \in \mathcal{P}_k$. The phase shifts of \mathcal{P}_k are set to align the channels for U_k , such that²

$$\Phi_k(x_k, y_k) = e^{-j(\angle h_{kk}(x_k, y_k) + \angle g_k(x_k, y_k))}. \quad (1)$$

This results in the coherent combining of received signal components for U_k at the destination. The BS estimates the cascaded CRIS channels of U_k through its designated partition \mathcal{P}_k , $h_{kk}g_k$, which it uses to adjust the CRIS phase shifts as in (1) [2], [3]. The angle of the cascaded channel is the sum of the individual channel angles. The signal reflections of U_k via partition $\mathcal{P}_i, \forall i \neq k$ are residual components with zero mean, as the phase shifts of \mathcal{P}_i are not optimized for U_k .

The received superimposed NOMA signal at the BS is thus

$$y = \sum_{k=1}^K \sum_{i=1}^K \sqrt{\frac{P_k \eta_k}{\nu_k}} \int_{x_i=0}^{W_i} \int_{y_i=0}^H h_{ki}(x_i, y_i) \times \Phi_i(x_i, y_i) g_i(x_i, y_i) dx_i dy_i s_k + n, \quad (2)$$

where P_k is the transmit power of U_k , s_k is the transmitted modulated symbol, ν_k is a scaling factor that normalizes s_k , $n \sim \mathcal{CN}(0, 2\sigma_n^2)$ is the additive white Gaussian noise, $\eta_k = d_{\text{ur},k}^{-\psi} d_{\text{rb}}^{-\psi}$ is the total path loss of the cascaded channel, $d_{\text{ur},k}$ is the distance of the U_k -CRIS link, d_{rb} is the distance of the CRIS-BS link, and ψ is the path-loss exponent.

The modulation symbol, $s_k \in \mathbb{C}$, is drawn from a square quadrature amplitude modulation (QAM) alphabet, \mathcal{S}_k , where the cardinality of \mathcal{S}_k is M_k , the modulation order of U_k . Both

the real and imaginary components of s_k can take values from the set $\{\pm 1, \pm 3, \dots, \pm \sqrt{M_k} - 1\}$. The scaling factor $\nu_k = 2(M_k - 1)/3$ is used to normalize s_k to unity.

The superimposed received signal in (2) can be rewritten as

$$y = \sum_{k=1}^K \left(\gamma_{kk} + \sum_{i \neq k} \gamma_{ki} \right) s_k + n, \quad (3)$$

where γ_{kk} is the optimized component of the effective channel of U_k , such that

$$\gamma_{kk} = \sqrt{\frac{P_k \eta_k}{\nu_k}} \int_{(x_k, y_k) \in \mathcal{P}_k} |h_{kk}(x_k, y_k)| |g_k(x_k, y_k)| dx_k dy_k, \quad (4)$$

while γ_{ki} is the random component of the effective channel of U_k , such that

$$\gamma_{ki} = \sqrt{\frac{P_k \eta_k}{\nu_k}} \int_{(x_i, y_i) \in \mathcal{P}_i} h_{ki}(x_i, y_i) e^{-j\angle h_{ii}(x_i, y_i)} |g_i(x_i, y_i)| dx_i dy_i. \quad (5)$$

The scalar value γ_{ki} represents the sum of the cascaded channels from U_k to the BS through all points in partition $\mathcal{P}_i, \forall i \neq k$, which can be estimated using a single pilot signal.³ This estimation introduces negligible pilot overhead compared to estimating all individual cascaded channels of U_k through all CRIS points in partition \mathcal{P}_k , whose pilot overhead scales linearly with the surface area of \mathcal{P}_k .

III. ANALYSIS OF THE RIS EFFECTIVE CHANNELS

In this section, we analyze the CRIS effective channels and derive terms required to obtain expressions for the BER. To facilitate the BER derivation, channel alignment is performed to align the phases of the effective channels of all users so that the received superimposed NOMA signal has a QAM-like constellation shape. This alignment is achieved by applying a phase shift of β_i to all points in partition \mathcal{P}_i , such that they cancel the imaginary components of all effective channels as

$$\Im \left(\sum_{i=1}^K \gamma_{ki} e^{j\beta_i} \right) = 0, \quad \forall k \in \{1, \dots, K\}. \quad (6)$$

To solve (6), the system of equations is transformed to a least-squares unconstrained minimization problem, as

$$\min_{\beta_1, \dots, \beta_K} \sum_{k=1}^K \left(\Im \left(\sum_{i=1}^K \gamma_{ki} e^{j\beta_i} \right) \right)^2. \quad (7)$$

Problem (7) can be solved by a standard nonlinear optimization solver, such as the trust-region or Levenberg–Marquardt algorithms. The solution always converges to a stationary minimal point where the value of the objective function is zero, as $\gamma_{kk} \gg \gamma_{ki}$, so γ_{kk} dominates the random components for small β_i . Thus, the aligned effective channel of U_k is

$$h_k^{\text{eff}} = \sum_{i=1}^K \gamma_{ki} e^{j\beta_i} \approx \gamma_{kk} + \sum_{i=1, i \neq k}^K \Re(\gamma_{ki}), \quad \forall k, \quad (8)$$

and the received signal becomes $y = \sum_{k=1}^K h_k^{\text{eff}} x_k + n$. As γ_{kk} and γ_{ki} are effectively uncorrelated⁴, the CF of h_k^{eff} is

$$\Phi_{h_k^{\text{eff}}}(z) = \Phi_{\gamma_{kk}}(z) \prod_{i \neq k} \Phi_{\Re(\gamma_{ki})}(z). \quad (9)$$

³Channel estimation methods for continuous surfaces are fast developing in the literature via approaches, such as reconstruction from discrete samples [10] and Gaussian process regression [11].

⁴As γ_{kk} and γ_{ki} are obtained by integrating over disjoint partitions, they become asymptotically uncorrelated. As W_k grows, inter-partition distances increase and the remaining cross-correlations average out to negligible values.

¹While physically realizing a perfect CRIS is challenging, hardware designs have recently been proposed to closely implement a continuous aperture surface [5]. This work provides a CRIS performance upper bound.

²This closed-form expression for the phase shifts of the CRIS reduces the complexity by significantly simplifying design and optimization.

The exact distributions of γ_{kk} and $\Re(\gamma_{ki})$ are intractable. We instead use the highly accurate gamma approximation for γ_{kk} and Gaussian approximation for $\Re(\gamma_{ki})$ [8], [9], giving

$$\Phi_{\gamma_{kk}}(z) \approx \frac{1}{(1-j\theta_k z)^{\alpha_k}}, \quad (10)$$

$$\Phi_{\Re(\gamma_{ki})}(z) \approx \exp\left(j\Re(\mathbb{E}[\gamma_{ki}])z + \frac{\text{Var}[\Re(\gamma_{ki})]z^2}{2}\right), \quad (11)$$

where $\theta_k = \frac{\text{Var}[\gamma_{kk}]}{\mathbb{E}[\gamma_{kk}]}$ is the gamma scale parameter and $\alpha_k = \theta_k \mathbb{E}[\gamma_{kk}]$ is the gamma shape parameter. Therefore, the first and second moments of γ_{kk} and $\Re(\gamma_{ki})$ are required.

A. First moments

Adapting [9, Eq. (23)], the first moment of γ_{kk} is

$$\begin{aligned} \mathbb{E}[\gamma_{kk}] &= \sqrt{\frac{P_k \eta_k}{\nu_k}} \int_{(x_i, y_i) \in \mathcal{P}_i} \mathbb{E}[|h_{kk}(x_k, y_k)|] \mathbb{E}[|g_k(x_k, y_k)|] dx_k dy_k, \\ &= \sqrt{\frac{P_k \eta_k}{\nu_k}} \frac{\pi}{4} W_k H. \end{aligned} \quad (12)$$

Since $\mathbb{E}[h_{ki}(x_k, y_k)] = 0$, $\mathbb{E}[\gamma_{ki}] = 0$.

B. Second moments

The second moment of γ_{kk} is

$$\text{Var}[\gamma_{kk}] = \mathbb{E}[\gamma_{kk}^2] - \mathbb{E}[\gamma_{kk}]^2.$$

As $\Re(\gamma_{ki})$ is zero-mean, and as both the real and imaginary components of γ_{ki} are identically distributed, we have

$$\text{Var}[\Re(\gamma_{ki})] = \frac{1}{2} \mathbb{E}[|\gamma_{ki}|^2].$$

The expression for $\mathbb{E}[\gamma_{kk}]$ was stated in (12), and the expressions for $\mathbb{E}[|\gamma_{kk}|^2]$ and $\mathbb{E}[|\gamma_{ki}|^2]$ are given below.

Proposition 1. Assuming isotropic correlation, $\mathbb{E}[\gamma_{kk}^2] = \Omega(k)$ and $\mathbb{E}[|\gamma_{ki}|^2] = \Omega(i)$, with $\Omega(x)$ given in (13) and

$$g_k(r_k) = {}_2F_1(-0.5, -0.5, 1, |\rho(r_k)|^2),$$

$$g_i(r_i) = \rho^2(r_i) {}_2F_1(-0.5, -0.5, 1, |\rho(r_i)|^2) {}_2F_1(0.5, 0.5, 2, |\rho(r_i)|^2),$$

with $r_k = \sqrt{(x_k - x'_k)^2 + (y_k - y'_k)^2}$ and $r_i = \sqrt{(x_i - x'_i)^2 + (y_i - y'_i)^2}$.

Proof. Substituting γ_{kk} with (4), $\mathbb{E}[\gamma_{kk}^2]$ can be expressed as

$$\begin{aligned} \mathbb{E}[\gamma_{kk}^2] &= \frac{P_k \eta_k}{\nu_k} \int_{(x_k, y_k) \in \mathcal{P}_k} \int_{(x'_k, y'_k) \in \mathcal{P}_k} \mathbb{E}[|h_{kk}(x_k, y_k)| |h_{kk}(x'_k, y'_k)|] \\ &\quad \times \mathbb{E}[|g_k(x_k, y_k)| |g_k(x'_k, y'_k)|] dx_k dy_k dx'_k dy'_k. \end{aligned}$$

Both expectations involve products of identically distributed correlated Rayleigh random variables with the same correlation function. Therefore, applying [12, Eq. (4.19)] yields

$$\mathbb{E}[\gamma_{kk}^2] = \frac{P_k \eta_k \pi^2}{16 \nu_k} \int_{(x_k, y_k) \in \mathcal{P}_k} \int_{(x'_k, y'_k) \in \mathcal{P}_k} g_k(x_k, y_k, x'_k, y'_k) dx_k dy_k dx'_k dy'_k. \quad (14)$$

with

$$g_k(x_k, y_k, x'_k, y'_k) = {}_2F_1(-0.5, -0.5, 1, |\rho(x_k, y_k, x'_k, y'_k)|^2).$$

Substituting γ_{ki} with (5), $\mathbb{E}[|\gamma_{ki}|^2]$ can be expressed as

$$\begin{aligned} \mathbb{E}[|\gamma_{ki}|^2] &= \frac{P_k \eta_k}{\nu_k} \int_{(x_i, y_i) \in \mathcal{P}_i} \int_{(x'_i, y'_i) \in \mathcal{P}_i} \mathbb{E}\left[e^{j(\mathcal{L}h_{ii}(x'_i, y'_i) - \mathcal{L}h_{ii}(x_i, y_i))}\right] \\ &\quad \times \mathbb{E}[h_{ki}(x_i, y_i) h_{ki}^*(x_i, y_i)] \mathbb{E}[|g_i(x_i, y_i)| |g_i(x'_i, y'_i)|] dx_i dy_i dx'_i dy'_i. \end{aligned}$$

As it is the product of two correlated random variables, $\mathbb{E}[h_{ki}(x_i, y_i) h_{ki}^*(x_i, y_i)] = \rho(x_i, y_i, x'_i, y'_i)$. For $\mathbb{E}[\gamma_{kk}^2]$, $\mathbb{E}[|g_i(x_i, y_i)| |g_i(x'_i, y'_i)|]$ can be found the same way as $\mathbb{E}[|g_k(x_k, y_k)| |g_k(x'_k, y'_k)|]$, whereas [12, Eq. (4.26)] gives $\mathbb{E}[e^{j(\mathcal{L}h_{ii}(x'_i, y'_i) - \mathcal{L}h_{ii}(x_i, y_i))}]$. Therefore,

$$\mathbb{E}[|\gamma_{ki}|^2] = \frac{P_k \eta_k \pi^2}{16 \nu_k} \int_{(x_i, y_i) \in \mathcal{P}_i} \int_{(x'_i, y'_i) \in \mathcal{P}_i} g_i(x_i, y_i, x'_i, y'_i) dx_i dy_i dx'_i dy'_i, \quad (15)$$

where

$$\begin{aligned} g_i(x_i, y_i, x'_i, y'_i) &= {}_2F_1(0.5, 0.5, 2, |\rho(x_i, y_i, x'_i, y'_i)|^2) \\ &\quad \times {}_2F_1(-0.5, -0.5, 1, |\rho(x_i, y_i, x'_i, y'_i)|^2) \rho^2(x_i, y_i, x'_i, y'_i). \end{aligned}$$

Both (14) and (15) are integrals of the same general form over different subsurfaces. This type of integral is solved in [9, Appendix C]. As isotropic correlation is assumed, the quadruple integrals can be transformed into a sum of single integrals over the distance between pairs of points, r , resulting in $\Omega(x)$ in (13). Substituting k and i as the argument x gives the final result for $\mathbb{E}[\gamma_{kk}^2]$ and $\mathbb{E}[|\gamma_{ki}|^2]$, respectively. ■

IV. PA AND RIS AREA SPLITTING-BASED OPTIMIZATION SCHEME FOR CRIS-NOMA

In this section, we use the expressions derived in Sec. III to obtain analytical expressions for the BER of each UE. We use these BER expressions to optimize the transmit powers, P_k , and the CRIS partition widths, W_k , to minimize the average BER of all UEs at the BS.⁵ From [8], the unconditional average BER of U_k for channel-aligned UL NOMA is

$$\text{BER}_{U_k} = \sum_{q=1}^{N_k} \frac{c_q}{2} + \frac{c_q}{\pi} \int_0^\infty \Re\left(\frac{j e^{-z^2/2}}{z} \Phi_{X_q}\left(\frac{z}{\sigma_n}\right)\right) dz, \quad (16)$$

where N_k is the total number of $Q(\cdot)$ functions in (16), a_{kq} and c_q are constants that depend on K and M_k , and $\Phi_{X_q}(z) = \prod_{k=1}^K \Phi_{h_k^{\text{eff}}}(a_{kq} z)$. The proposed optimization strategies aim to eliminate the BER floors inherent in SIC-based UL PD-NOMA systems. Using (16), we derive optimized values of P_k and W_k for each UE that minimize the average (sum) BER⁶ of all users while satisfying individual UL transmit power constraints. The optimization is more stable and accurate when expressed in the log-log domain, where both P_k and the cost function are expressed in dB. This transformation leads to

⁵The extension to the multi-antenna BS case follows the same design and BER analysis as the single-antenna scenario. The key difference is the introduction of a BS receive combiner, which can be jointly optimized with the CRIS phase shifts via alternating maximization. The resulting, empirically characterized, effective channel statistics can then be used in the same BER-based power allocation procedure as in the single-antenna case.

⁶Note that we minimize the average (sum) of the BERs of the UEs to ensure that no UE's BER remains high, as a single large BER would dominate the sum. This formulation is simpler than minimizing the maximum BER, however, we compare against the min-max solution in the results in Sec. V.

$$\Omega(x) = \frac{P_x \eta_x \pi^2}{4\nu_x} \left(\int_0^H r_x g_x(r_x) \left[W_x H \frac{\pi}{2} - (W_x + H)r_x + \frac{r_x^2}{2} \right] dr_x + \int_H^{W_x} r_x g_x(r_x) \left[W_x H \sin^{-1} \left(\frac{H}{r_x} \right) + W_x \sqrt{r_x^2 - H^2} - W r_x - \frac{H^2}{2} \right] dr_x \right. \\ \left. - \int_H^{\sqrt{W_x^2 + H^2}} r_x g_x(r_x) \left[W_x H \left(\cos^{-1} \left(\frac{W_x}{r_x} \right) - \sin^{-1} \left(\frac{H}{r_x} \right) \right) + \frac{W_x^2 + H^2 + r_x^2}{2} - W_x \sqrt{r_x^2 - H^2} - H \sqrt{r_x^2 + W_x^2} \right] dr_x \right), \quad (13)$$

a smoother objective function and faster convergence with gradient descent-based methods. The UL PA problem is thus

$$\min_{P_k, W_k} 10 \log_{10} \left(\sum_{k=1}^K \text{BER}_{U_k} \left(10^{\frac{P_1}{10}}, \dots, 10^{\frac{P_K}{10}}, W_1, \dots, W_K \right) \right), \quad (17a)$$

$$\text{s.t. } P_k \leq P_{\text{dBm}}^{\max}, \quad \forall k, \quad (17b)$$

$$0 \leq W_k \leq W, \quad \forall k, \quad (17c)$$

$$\sum_{k=1}^K W_k = W, \quad (17d)$$

where P_{dBm}^{\max} is the maximum available UL transmit power in dBm and BER_{U_k} is given in (16). The optimization parameters P_k and W_k in (17a) come from $\Phi_{X_q}(\cdot)$ in (16), which is a function of $\Phi_{h_k^{\text{eff}}}(\cdot)$ which in turn is a function of $\Phi_{\gamma_{kk}}(\cdot)$ and $\Phi_{\Re(\gamma_{ki})}(\cdot)$ in (9), and both are functions of P_k and W_k .

To handle the constraints, (17) is transformed into an unconstrained optimization problem by constructing the Lagrangian,

$$L(\mathbf{p}, \mathbf{w}, \boldsymbol{\xi}, \boldsymbol{\delta}, \omega) = f(\mathbf{p}) + \sum_{k=1}^K \xi_k \max(0, P_k - P_{\text{dBm}}^{\max}) \\ + \sum_{k=1}^K \delta_k \max(0, W_k - W) + \omega \left(\sum_{k=1}^K W_k - W \right)^2, \quad (18)$$

where $\boldsymbol{\xi} = [\xi_1, \dots, \xi_K]^T$, $\boldsymbol{\delta} = [\delta_1, \dots, \delta_K]^T$ and ω are the Lagrange multipliers, $f(\cdot)$ is the cost function in (17), $\mathbf{p} = [P_1, \dots, P_K]^T$ and $\mathbf{w} = [W_1, \dots, W_K]^T$. The optimization problem is solved iteratively by setting low initial values for the penalty weights $\boldsymbol{\xi}$, $\boldsymbol{\delta}$ and ω . Next, the Lagrangian in (18) is minimized in each iteration using a gradient descent-based method as it is continuous and has continuous first derivatives. The penalty weights are increased in each iteration if the corresponding constraints are violated. After multiple iterations, the algorithm converges to the minimum weights at which (17a) is minimized while the constraints are satisfied.

The computational complexity of problem (17) is dominated by the cost of the gradient evaluation of the Lagrangian in (18). The Lagrangian gradient is approximated via forward finite differences, requiring $\mathcal{O}(K)$ additional function evaluations per iteration. The cost of one Lagrangian evaluation C_L is dominated by the computation of $\sum_{k=1}^K \text{BER}_{U_k}$. With I inner and J outer iterations, the computational complexity of the proposed algorithm is $\mathcal{O}(JIKC_L)$.

The complexity of computing C_L is dominated by calculating the BER expression in (16). To reduce the cost, the Gaussian hypergeometric function used to calculate the second moments of γ_{kk} and γ_{ki} is approximated using the polynomial series expansion in [13, Eq. (15.2.1)] truncated to L terms. This expansion is very accurate when $|z| < 1$, which is true here as z is the squared isotropic correlation. Thus, a value such as $L = 6$ is sufficient for a highly accurate approximation.

V. SIMULATION RESULTS

Figures 2 and 3 plot the average BER of each UE against the transmit power for a 2 and 3 UE system, respectively.

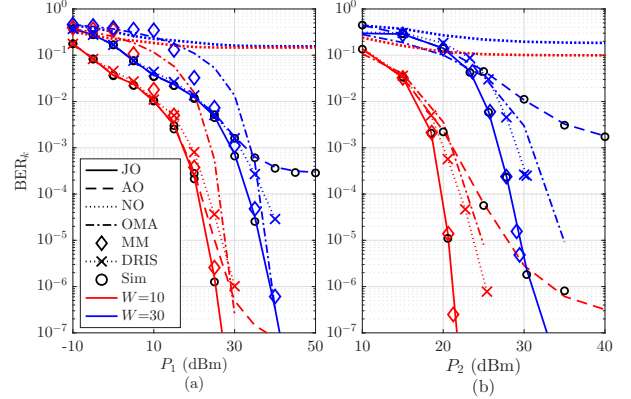


Fig. 2. BERs for two-user systems: (a) U_1 , (b) U_2 .

The noise variance is $\sigma_n^2 = 10^{-9}$ mW [14], the path loss exponent is $\psi = 2.2$, $d_{\text{rb}} = 30$ m, $d_{\text{ur},1} = 20$ m and $d_{\text{ur},3} = 220$ m. In Fig. 2, $d_{\text{ur},2} = 50$ m and in Fig. 3, $d_{\text{ur},2} = 70$ m. Due to its close proximity to the CRIS, U_1 employs 64-QAM to increase throughput, while U_2 and U_3 employ 16-QAM. The CRIS height is fixed at $H = 5\lambda$, where λ is the signal wavelength, while the width, W , varies across each figure. The carrier frequency used in the simulations is $f = 28$ GHz. The sinc correlation model is used, such that $\rho(x_i, y_i, x_k, y_k) = \text{sinc}(\frac{2}{\lambda} \sqrt{(x_i - x_k)^2 + (y_i - y_k)^2})$. We compare the performance of the CRIS with a DRIS with an element spacing of $\lambda/2$, and having the same surface area for a fair comparison.

Each sub-figure compares four methods for a single UE: the joint optimization approach in (17) (JO), optimization only over CRIS area partitions (AO), no optimization (NO), and a time-slotted OMA baseline. In scenarios where the CRIS partition size or transmit power is not optimized, the resource is shared equally among UEs. The four methods are applied and compared under different CRISs sizes in each figure. Figure 2 also shows results for the minimization of the maximum BER (MM), as a comparison to minimizing the average BER in (17a).

For a fair comparison, the modulation order of U_k in the OMA system is chosen as $M_k^{\text{OMA}} = (M_k^{\text{NOMA}})^K$, such that the number of bits per symbol for OMA is that of NOMA multiplied by K . This ensures that both systems achieve the same overall bit rate. Moreover, the transmit power of U_k in the OMA system is scaled by a factor of K so that the average transmit power is identical in OMA and NOMA. To maintain fairness in terms of channel estimation overhead, in the OMA scenario, we assume that the BS only has knowledge of \mathcal{P}_k for U_k , as in the NOMA case, rather than of the entire CRIS.

Figures 2 and 3 demonstrate excellent agreement between the analytical results using (16) and simulations. This confirms the accuracy of our approximation of $\Phi_{h_k^{\text{eff}}}(z)$, which enables the tractable BER expression required for optimization.

Without optimization, NOMA exhibits persistent error floors

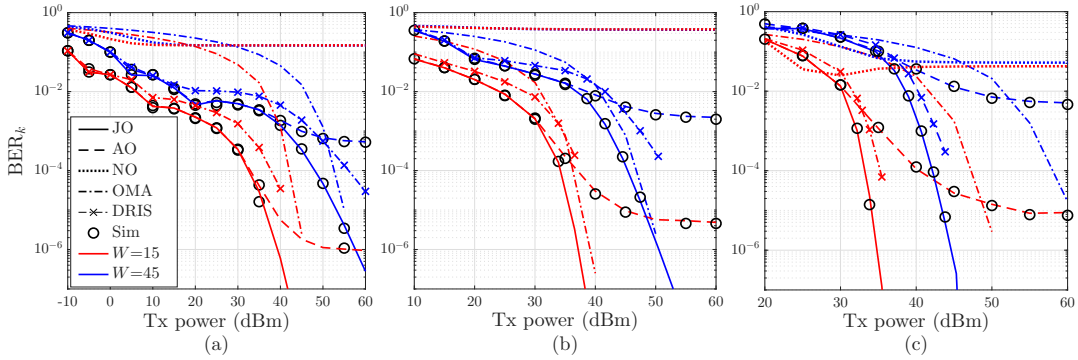


Fig. 3. BERs for three-user systems: (a) U_1 , (b) U_2 , (c) U_3 .

due to employing SIC. Residual errors from SIC persist even as the transmit power increases and noise impact diminishes, resulting in the observed error floor. This floor exceeds 0.1 for the strongest UE, meaning over 1 in 10 bits are incorrectly detected, highlighting the need for optimization for reliable operation. Equal PA overlooks variations in channel quality among UEs, reducing the effectiveness of SIC. Increasing the CRIS size without proper optimization yields limited BER improvement, as inter-user interference (IUI) remains significant. Optimizing the CRIS partitions while maintaining equal transmit PA among UEs leads to significant improvements in BER performance. This gain is especially evident for larger CRIS sizes and for stronger UEs as they are assigned larger sections of the CRIS since they are first decoded in the SIC order. However, the error floor is not completely eliminated. This occurs because, at high signal-to-noise ratio (SNR) levels, the optimization algorithm allocates larger CRIS partitions to the stronger UE and smaller CRIS partitions to the weaker UEs to suppress IUI and mitigate the error floor. However, the smaller partition sizes reduce channel hardening for the weaker UEs, and this increased variability degrades its BER performance. The error floor emerges when further improvements in the BER of the stronger UEs come at the expense of equivalent BER degradation of the weaker UEs, limiting the overall performance.

The joint optimization of the CRIS partition and PA completely removes the error floor for BERs of at least 10^{-7} . Optimizing PA complements CRIS partitioning by enabling interference reduction without sacrificing channel hardening. PA manages IUI independently in the PD, enabling interference reduction without reducing CRIS resources. This approach preserves or even enhances channel hardening while simultaneously improving BER performance. Figure 2 also shows that minimizing the maximum BER and minimizing the average BER in (17a) converge to the same result at high SNR, but (17a) provides better performance in the low SNR region. The superiority of the CRIS over a DRIS is also clear.

Optimized NOMA outperforms OMA in all scenarios studied by enabling multiple UEs to simultaneously access the full resource block without incurring excessive IUI. The extra resource per user allows NOMA to use lower-order modulation schemes, reducing the likelihood of symbol errors. The JO of CRIS partitioning and PA is very effective at managing IUI, allowing the benefits of increased resource sharing to outweigh interference and provide superior BER performance.

VI. CONCLUSIONS

This paper investigated a CRIS-enabled UL NOMA system under spatially correlated fading. We analyzed the effective channels and derived BER expressions using a CF approximation. A joint PA and CRIS partitioning optimization scheme was developed to minimize the average BER and mitigate the BER floors caused by IUI. Simulation results confirmed the accuracy of the analysis and the superiority of the optimized CRIS-NOMA scheme over both a traditional OMA system, and a NOMA system involving a DRIS, highlighting the potential of combining CRIS and NOMA in future networks.

REFERENCES

- [1] O. Maraqa *et al.*, "A survey of rate-optimal power domain NOMA with enabling technologies of future wireless networks," *IEEE Commun. Surv. Tutor.*, vol. 22, no. 4, pp. 2192–2235, Aug. 2020.
- [2] A. P. Chrysologou, A.-A. A. Boulogeorgos, N. D. Chatzidiamantis, and A. Alexiou, "Outage analysis of holographic surface assisted downlink terahertz NOMA," in *Proc. IEEE GLOBECOM*, Dec. 2022.
- [3] A. P. Chrysologou, A.-A. A. Boulogeorgos, and N. D. Chatzidiamantis, "When THz-NOMA meets holographic reconfigurable intelligent surfaces," *IEEE Commun. Lett.*, vol. 27, no. 9, pp. 2516–2520, Sep. 2023.
- [4] D.-T. Vo *et al.*, "Holographic reconfigurable intelligent surface-aided downlink NOMA IoT networks in short-packet communication," *IEEE Access*, vol. 12, pp. 65 266–65 277, May 2024.
- [5] Y. Liu *et al.*, "CAPA: Continuous-aperture arrays for revolutionizing 6G wireless communications," *IEEE Wireless Commun.*, vol. 32, no. 4, pp. 38–45, Aug. 2025.
- [6] T. Hou *et al.*, "Transmission power optimization for continuous-aperture array (CAPA)," *IEEE Trans. Commun.*, vol. 74, pp. 2641–2656, Jan. 2026.
- [7] R. Deng *et al.*, "Reconfigurable holographic surface-enabled multi-user wireless communications: Amplitude-controlled holographic beamforming," *IEEE Trans. Wireless Commun.*, vol. 21, no. 8, pp. 6003–6017, Aug. 2022.
- [8] M. AlaaEldin *et al.*, "RIS-enabled multi-user M -QAM uplink NOMA systems: Design, analysis and optimization," *arXiv:2503.03972*, Mar. 2025.
- [9] A. S. Inwood, M. AlaaEldin, P. J. Smith, and M. Matthaiou, "Performance characterization of continuous reconfigurable intelligent surfaces," in *Proc. IEEE ICC*, June 2025.
- [10] W. Kiat New *et al.*, "Channel estimation and reconstruction in fluid antenna system: Oversampling is essential," *IEEE Trans. Wireless Commun.*, vol. 24, no. 1, pp. 309–322, Jan. 2025.
- [11] Z. Zhang, J. Zhu, L. Dai, and R. W. Heath, Jr., "Successive Bayesian reconstructor for channel estimation in fluid antenna systems," *IEEE Trans. Wireless Commun.*, vol. 24, no. 3, pp. 1992–2006, Mar. 2025.
- [12] K. S. Miller, *Complex Stochastic Processes: An Introduction to Theory and Application*. Addison-Wesley, 1974, p. 76–100.
- [13] National Institute of Standards and Technology, "Digital Library of Mathematical Functions." Accessed: Jan. 28, 2026. [Online]. Available: <https://dlmf.nist.gov>
- [14] Q. Wu and R. Zhang, "Intelligent reflecting surface enhanced wireless network via joint active and passive beamforming," *IEEE Trans. Wireless Commun.*, vol. 18, no. 11, pp. 5394–5409, Nov. 2019.